Report on Landsat 8 and Sentinel-2B observations of the Nord Stream 2 pipeline methane leak

Matthieu Dogniaux[1], Joannes D. Maasakkers[1], Daniel J. Varon[2] and Ilse Aben[1]
[1]SRON Netherlands Institute for Space Research, Leiden, The Netherlands
[2]School of Engineering and Applied Science, Harvard University, Cambridge, USA

5   **Corresponding author:** Matthieu Dogniaux
Email: M.Dogniaux@sron.nl

Report on Landsat 8 and Sentinel-2B observations of the Nord Stream 2 pipeline methane leak

Matthieu Dogniaux[1], Joannes D. Maasakkers[1], Daniel J. Varon[2], and Ilse Aben[1]

[1]SRON Netherlands Institute for Space Research, Leiden, The Netherlands
[2]School of Engineering and Applied Science, Harvard University, Cambridge, 02138, USA

Correspondence: Matthieu Dogniaux (M.Dogniaux@sron.nl)

Abstract. In late September 2022, explosions of the Nord Stream pipelines caused what could be the largest anthropogenic methane leak ever recorded. We report on Landsat 8 (L8) and Sentinel-2B (S-2B) observations of the sea foam patch produced by the Nord Stream 2 (NS2) leak located close to Bornholm Island, acquired on September 29th and 30th, respectively. Usually, reflected sunlight over sea is insufficient for these Earth-imagers to observe any methane signal in ~~nadir-vewing~~ nadir-viewing geometry. However, the NS2 foam patch observed here is bright enough to possibly allow the detection of methane above it. We apply the Multi-Band Single-Pass (MBSP) method to infer methane enhancement above the NS2 foam patch and then use the Integrated Mass Enhancement (IME) method in ~~an~~ a Monte Carlo ensemble approach to estimate methane leak rates and their uncertainties. This very specific NS2 observation case challenges some of MBSP and IME implicit ~~hypotheses~~assumptions, and thus calls for customized calibrations: (1) for MBSP, we perform an empirical calibration of sea foam albedo spectral dependence by using sea foam observations in ship trails, and (2) for IME, we yield a tailored effective wind speed calibration that accounts for a partial plume observation, as methane enhancement may only be seen above the NS2 sea foam patch. ~~Due to large uncertainties,~~ Our comprehensive uncertainty analysis yields large methane leak rate uncertainty ranges that include zero, with a best estimate of 501 ± 521 t/hr. Thus, no firm conclusion can be drawn from the single or combined overpasses of L8 and S-2B. ~~However, if we opportunistically assume that the L8 and S-2B~~ Within all our Monte Carlo ensembles, positive methane leak rates ~~are independent, we obtain a positive leak detection with a weak confidence, showing an averaged dual-overpass~~ ~~(~~have higher probabilities ($79-88\%$) than negative ones ($12-21\%$), thus indicating that L8 and S-2B ~~combined) NS2 methane leak rate of 415 ± 321 t/hr~~likely captured a methane-related signal. Overall, ~~our work illustrates how implicit method hypotheses need to be considered and compensated for in unusual observation cases such as this one~~we see our work both as a nuanced analysis of L8 and S-2B contributions to quantifying the NS2 leak emissions and as a methodological cautionary tale that builds insight on MBSP and IME sensitivities.

1 Introduction

From September 26th to October 2nd, 2022, leaks occurred on the Nord Stream (NS) and Nord Stream 2 (NS2) pipelines in the Baltic Sea. They caused intensive bubbling and extensive foam patches at the sea surface, as well as methane emissions that could be one of the strongest methane leak events ever recorded (Sanderson, 2022). The Southern NS2 sea foam patch close

to Bornholm Island was observed on September 29th and 30th by Landsat 8 and Sentinel-2B (respectively), two Earth-imaging satellites that are sensitive to large methane point sources (Varon et al., 2021). We report on those two observations, and exhibit the challenges they come with to evaluate the NS2 methane leak rate.

Anthropogenic methane emissions are the second largest contributor to human-induced climate change, and their drastic reduction is required to keep global warming below $1.5°C$ or $2.0°C$ (IPCC, 2021). In the past decade, developments in space-based methane observation have had a transformative impact on methane super-emitter detection and monitoring, and can contribute to track progress towards the Paris Agreement goals (e.g. Nisbet et al., 2020). Among them, the TROPOspheric Monitoring Instrument (TROPOMI, Veefkind et al., 2012; Lorente et al., 2021) measures back-scattered sunlight in the short-wave infrared (SWIR) around 2.3 μm at 0.25 nm resolution, at a moderate 5.5×7 km^2 spatial resolution at nadir and with daily global coverage. Global methane concentrations maps are drawn from these measurements using a full-physics approach which accounts for geophysical variables besides methane (e.g. albedo, water vapour, aerosol optical depth, etc) that could interfere in the retrieval process (Lorente et al., 2021). Its observations have been successfully used to detect and estimate anthropogenic methane emissions arising from various point or localized sources (e.g. Pandey et al., 2019; Lauvaux et al., 2022; Schuit et al., 2023). SWIR satellite instruments with higher spatial resolution (few tens of meters) have proved complementary by enabling the identification of methane emission sources at facility-scale. These notably include the methane-dedicated GHGSat constellation (Jervis et al., 2021) and Earth-imagers such as Sentinel-2 or Landsat 8. Earth-imagers are not spectrally resolved like TROPOMI and were not originally designed to measure greenhouse gases. However, under the right conditions (bright, quasi-homogeneous land surface), their methane sensitive bands ($\sim$ 100-200 nm in width) can be repurposed to retrieve large methane concentration enhancements and image point source emission plumes (e.g. Varon et al., 2021; Irakulis-Loitxate et al., 2022b). Like any other SWIR instrument, these Earth-imagers do not typically offer coverage over water bodies, because the water albedo is too dark at nadir pointing. However, sun-glint observations over sea can allow methane plume detection with these satellites as well (Irakulis-Loitxate et al., 2022a).

When the NS and NS2 leaks occurred, and in the following week, TROPOMI was not able to acquire exploitable data over land in the Baltic Sea vicinity due to cloudiness. However, thanks to their finer spatial resolution, Landsat 8 (L8) and Sentinel-2B (S-2B) have been able to perform nadir-pointing observations showing the Southern NS2 leak on September 29th and 30th, respectively. They did not benefit from sun glint, but the bright foam patch produced by the bubbling leak at the sea surface reflected enough sunlight to consider using the observations, and assess whether a methane signal can be sensed. Besides L8 and S-2B, GHGSat could point their instruments towards the same NS2 leak on September 30th and observe a methane emission plume in glint geometry twice (GHGSat, 2022). After initial Twitter reports by the International Methane Emissions Observatory (IMEO, 2022), Jia et al. (2022) published results for the Sentinel-2B observation, acknowledging significant uncertainties in their methodology regarding the spectral reflectance of bubbles and the partial imaging of the methane plume.

This work first aims to show how Landsat 8 and Sentinel-2B observations of the Nord Stream 2 leak challenge implicit ~~hypotheses~~ assumptions in methods usually applied for Earth-imager methane plume analysis and emission rate quantification. It then proposes to account for identified issues by using customized calibrations, and to assess the possibility of using Landsat 8 and Sentinel-2B to sense and quantify methane emissions from the Nord Stream 2 leak.

This paper is structured as follows: Section 2 describes general aspects about the materials and methods used in this work as well as Nord Stream 2 specific calibrations. Section 3 presents the obtained methane leak rates. Finally, Section 4 highlights the conclusions of this work.

2 Materials and methods

This section describes general aspects of the data and methods used here, as well as the custom calibrations that are necessary to adapt them to this singular Nord Stream 2 observation case.

2.1 Landsat 8 and Sentinel-2B satellite observations

2.1.1 General aspects

Landsat 8 (hereafter L8) is an Earth-imaging satellite with a swath of 185 km and a revisit time of 16 days. It measures reflected sunlight over 10 different spectral bands located in the visible, short-wave infrared (SWIR) and thermal infrared, with spatial resolutions ranging from 15 to 100 m (Roy et al., 2014).

The Copernicus Sentinel-2 mission comprises two Earth-imaging satellites (Sentinel-2A and Sentinel-2B, hereafter S-2B) with a swath of 290 km and revisit time of 10 days each, and aims to monitor changes on our Earth's surface. They measure reflected sunlight over 12 different spectral bands located in the visible and SWIR, with spatial resolutions ranging from 10 to 60 m (Drusch et al., 2012).

Here, we use Top Of the Atmosphere (TOA) reflectance data observed by L8 and S-2B for two methane sensitive SWIR spectral bands around 1.6 μm (bands 6 and 11 for L8 and S-2B, respectively) and 2.2 μm (bands 7 and 12 for L8 and S-2B, respectively). These L8 and S-2B SWIR observations have spatial resolutions of 30 and 20 m, respectively.

2.1.2 Nord Stream 2 leak observations

Figure 1 shows L8 and S-2B TOA reflectance observations of the NS2 methane leak (top panels) and exhibits, using simple empirically-determined thresholds (see Supplements), the different pixel types (dark still sea, NS2 leak, cloud) included in the images by comparing s_1 and s_2 TOA reflectance values (bottom panels). The L8 image acquired on September 29th, 2022, is composed of the bubbling sea foam patch at its center, surrounded by dark still sea and cloud pixels. The S-2B image acquired on September 30th, 2022 is much cleaner and only includes the NS2 bubbling sea foam patch at its center, surrounded by dark still sea pixels.

2.2 Methane enhancement retrieval: the Multi-Band Single-Pass (MBSP) method

We use the Multi-Band Single-Pass (MBSP) method to retrieve local methane column enhancements from Earth imager observations. We first describe MBSP and its standard calibration approach, and then show how this specific NS2 case study calls for a custom calibration.
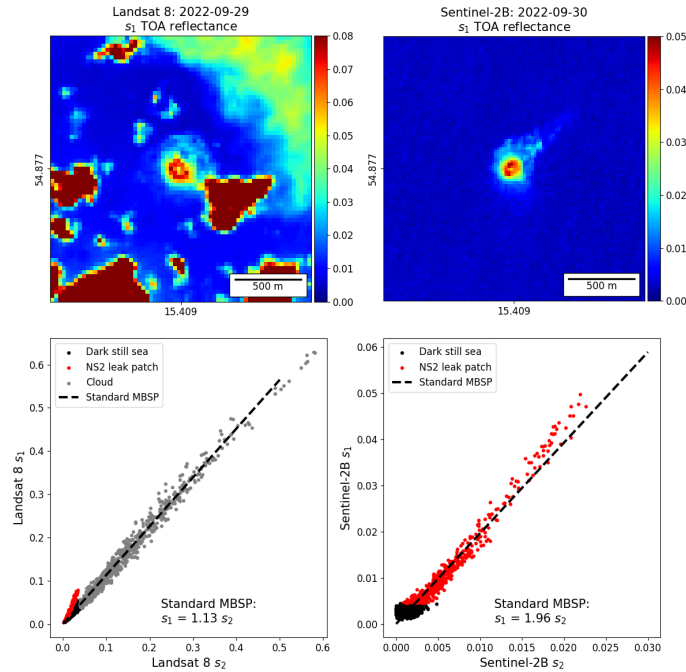
Figure 1. Landsat 8 (left, September 29$^{\text{th}}$ 2022) and Sentinel-2B (right, September 30$^{\text{th}}$ 2022) images of the Nord Stream 2 leak for s_1 (top), and s_1 and s_2 TOA reflectance comparisons depicting different pixel natures and showing the standard MBSP c calibration line (bottom). The pixel natures of dark still sea (black), clouds (grey) and NS foam patch (red, all influenced by the methane leak) are separated using empirically determined thresholds given in the Supplements. The standard MBSP calibration (dashed line) is provided here to illustrate why it proves to be unsuitable for this specific NS2 case, as detailed in Sect. 2.2.2.

2.2.1 General description

The TOA reflectance data can be used to retrieve atmospheric methane concentration enhancements with the Multi-Band Single-Pass (MBSP) method, first proposed by Varon et al. (2021). It relies on the relative change in TOA reflectance ΔR between two spectral bands s_1 (around 1.6 μm, low sensitivity to methane) and s_2 (around 2.2 μm, strong sensitivity to methane) computed as:

$$\Delta R = \frac{c \times s_2 - s_1}{s_1} \tag{1}$$

with c, a linear calibration coefficient fitted on all the pixels included in the target image, to account for any non-methane-related spectral effects between bands s_1 and s_2, most importantly the spectral dependence of the albedo. This calibration strategy was proposed with the MBSP method by Varon et al. (2021), and implicitly assumes that image-wide pixels are representative of the surface characteristics expected below the (potential) methane plume. Hereafter, we will refer to this "naïve" calibration strategy as the "standard MBSP calibration". The rationale of MBSP is that deviations in the methane-sensitive s_2 band from the

expected s_1/s_2 ratio (captured in the fitted c coefficient) are interpreted as methane enhancements. Pixels with $\Delta R < 0$ relate to higher than expected atmospheric absorption and yield positive methane enhancements. The translation of ΔR to methane enhancements is performed using pre-computed look-up tables, generated through radiative transfer simulations. Here, they are based on the 2020 version of the HITRAN spectroscopic database (Gordon et al., 2022), rely on a 21-layer atmospheric model representative of mid-latitudes and include the impact of the solar zenith angle.

2.2.2 Empirical calibration of the spectral dependence of sea foam reflectance in MBSP

Here, we seek to determine whether a methane enhancement signal can be retrieved from L8 and S-2B images of the NS2 sea foam patch. No methane signal can be expected to be visible over the dark still sea or the clouds. Consequently, considering the general description of MBSP given in Sect. 2.2.1, properly constraining the spectral dependence of sea foam albedo between s_1 and s_2 is critical to obtain non-biased methane enhancements through MBSP.

Whitlock et al. (1982) and Koepke (1984) show that we expect a ~~TOA~~ reflectance ratio s_1/s_2 over sea foam of about 2 or slightly lower (graphical reading). However, the only pixels representative of sea foam that can be observed in L8 and S-2B images of the NS2 leak are the ones caused by the leak itself, above which we also expect a possible methane enhancement signal. Unlike a land image, it is thus not possible to assess whether the standard MBSP calibration can separate the spectral impact of methane from the spectral dependence of the albedo for this specific NS2 case. This is particularly noticeable in Fig. 1 for the S-2B image, where the standard MBSP calibration is driven by the NS2 sea foam patch ($c = 1.96$). This issue similarly applies to the L8 NS2 observation, that also features an additional complication: very bright clouds are present in the image, which in this case drive the standard MBSP calibration ($c = 1.13$). ~~The~~ Thus, the standard MBSP calibration lines included in Fig. 1 illustrate why the NS2 observation case, that relies on a small sea foam patch ~~thus~~, calls for an external calibration of the spectral dependence of sea foam albedo.
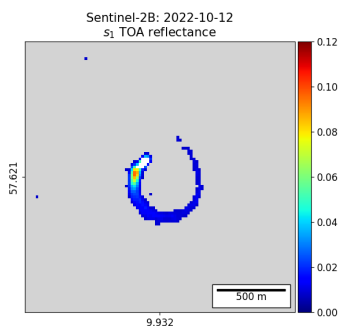
Figure 2. Example of sea foam observation in the Sentinel-2B image of a ship trail ~~.~~ acquired on October 12th, 2022. Dark still sea and ship pixels have been removed and are shown in grey and white, respectively. They are also excluded from the sea foam albedo spectral dependence results presented later in Sect. 2.2.2 and in the Supplements.

We therefore empirically constrain the spectral dependence of sea foam albedo by using sea foam observations in ship trails unaffected by methane plumes. We treat each satellite separately in order to account for their different instrumental characteristics. By visual inspection of RGB Sentinel-2 and Landsat data on the EO Browser of Sentinel-Hub (2023), we gather 27 and 38 images of ship trails for L8 and S-2B, respectively, located in the North and Baltic Seas from September and October 2022. For each of these images, we separate ship and sea foam pixels from the dark still sea pixels by using an empirically determined threshold τ_1, such that $s_1 > \tau_1$; and then separate sea foam from ship pixels by applying a second empirically determined threshold τ_2, such that $s_2 < \tau_2$ (Supplement Tables 2 and 3). Figure 2 shows an example of sea foam pixels extracted from an S-2B ship trail image. For each image, using sea foam pixels only, we perform a least-squares linear fit (with an intercept set to zero) of s_1 as a function of s_2 to determine c_i, the coefficient describing the spectral dependence of sea foam albedo for the i-th image (see individual ~~fits~~ c_i values and fits obtained for each ship trail observation in the Supplements). For L8 and S-2B separately, we then compute $\bar{c}$ as the mean of the individual calibrations. Figure 3 presents the results of this satellite-specific empirical calibration of the spectral dependence of sea foam albedo. We obtain $\bar{c} = 1.96 \pm 0.23$ and $\bar{c} = 1.91 \pm 0.22$ for L8 and S-2B, respectively. These ~~are~~ Top-of-the-Atmosphere reflectance ratios are overall consistent with results presented by Whitlock et al. (1982) and Koepke (1984) that were measured on the ground. Comparing the S-2B result to the slightly higher standard MBSP calibration ($c = 1.96$) also confirms the above mentioned hypothesis that the standard calibration may have captured some methane signal. Indeed, for given fixed $\{s_1, s_2\}$ values, a decrease in the spectral dependence calibration coefficient c (compared to the standard calibration) reduces $\Delta R = (c s_2 - s_1)/s_1$, which translates to an increase of methane enhancement ~~through~~ via the use of MBSP.
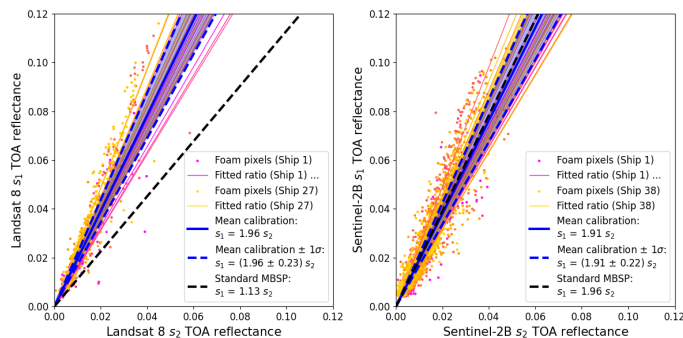
Figure 3. Empirically determined sea foam albedo spectral dependence between s_1 and s_2 for Landsat 8 (left) and Sentinel-2B (right). Sea foam pixels for all ship images are depicted (dots with different colors indicating different ships, the legend only includes elements for the first and last images), along with their respective calibration slopes (thin lines, each is detailed in the Supplements, the legend only includes elements for the first and last images). ~~The~~ These enable the computation of the mean and 1-σ standard deviation of the empirically determined sea foam albedo spectral dependence ~~are shown~~ (thick full and dashed blue lines)~~, along with the~~. The standard MBSP calibration (thick dashed black line) is also shown.
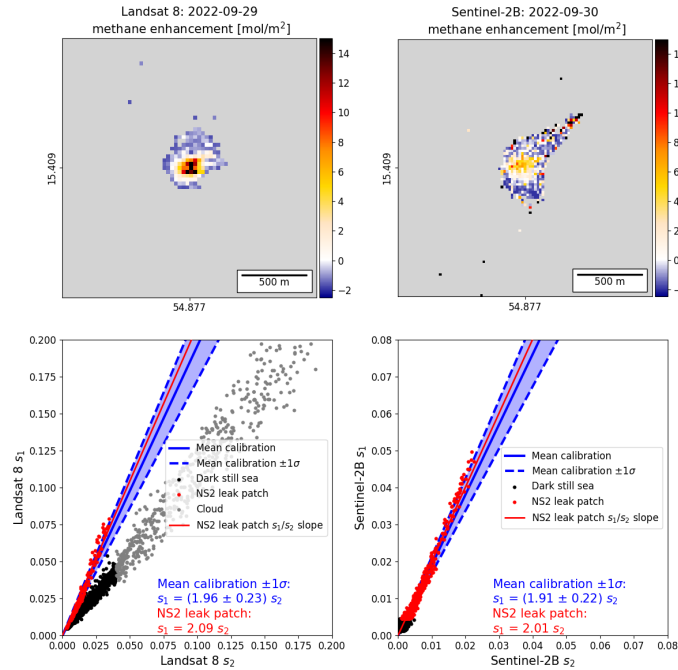
Figure 4. Methane enhancement results obtained through MBSP for Landsat 8 (top left, September 29th 2022) and Sentinel-2B (top right, September 30th 2022), pixels not belonging to the foam patch have been filtered out and shown in grey. Comparisons of s_1 and s_2 TOA reflectance (bottom) depicting different pixel types and showing the empirically determined spectral dependence of sea foam albedo (thick blue line, the individual ship trail observations underlying this result are shown in Fig. 3 and in supplementary Tables S2 and S3 for L8 and S-2B, respectively), and the s_1/s_2 ratio observed over the NS2 sea foam patch (red line). The higher slopes shown by the s_1/s_2 ratios (red) compared to the empirical calibrations (blue) are driven by the brightest pixels at the center of the sea foam patch that offer a better signal-to-noise ratio to observe methane absorption than darker pixels.

MBSP can then be applied using these newly determined empirical calibrations (computing ΔR using $\bar{c}$). Figure 4 shows the methane enhancements obtained with the satellite-specific $\bar{c}$ calibration values, and how s_1 and s_2 TOA reflectance values compare to them. For the L8 observation of the NS2 leak, the sea foam patch pixels show an s_1/s_2 ratio of 2.09 (red line), which is slightly higher than the average empirical calibration of the L8 sea foam albedo spectral dependence ($\bar{c} = 1.96 \pm$

150   0.23), but comprised within its $\pm 1\sigma$ uncertainty interval. This ship-based $\bar{c} - s_1/s_2$ negative difference overall translates to positive methane enhancement through MBSP. On average, we obtain L8 methane enhancement values ranging from -2.5 to 15 mol/m^2. Negative enhancements are associated with pixels falling right of the s_1/s_2 empirical calibration line (low TOA reflectance values, at the sea foam patch edges), and positive enhancements are associated with pixels falling left of the

155   empirical calibration line (high TOA reflectance values, at the sea foam patch center). The S-2B observation is similar but exhibits more noise, overall showing enhancements from -2.5 mol/m^2 on the sea foam patch edges to about 8 mol/m^2 at its brighter center.

2.3   Emission rate quantification: the Integrated Mass Enhancement (IME) method

We use the Integrated Mass Enhancement (IME) method to quantify the methane emission rate from local methane column
enhancement retrievals that show an emission plume. Here, we first explain why we choose the IME method and how it works,
then we explain why this specific NS2 case study also calls for a custom calibration for the IME method.

2.3.1   General description

If a plume is observed in ~~the~~ an image resulting from MBSP, the associated emission rate can be quantified using ~~the~~ different
approaches such as the Gaussian plume inversion (GP), source pixel (SP), Cross-Section flux (CSF) and Integrated Mass
Enhancement (IME) methods (Varon et al., 2018). Because GP and SP are not suited for the quantification of plumes detected
using high-resolution satellite observations, and the CSF relies on several transects drawn on an extended downwind plume,
we use the IME method. This method was first proposed by Frankenberg et al. (2016) and its calibration and operational use
was improved by Varon et al. (2018). Given a plume, the IME method relates the emission rate Q to the plume's total methane
mass and its residence time in the atmosphere. We have:

$$Q = \frac{U_{\text{eff}}}{L} \sum_i \Delta X_{CH_4 i} \times a_i \qquad (2)$$

with U_{eff}, the effective wind speed transporting the plume, $L = \sqrt{\sum_i a_i}$ the plume ~~length~~extent, $X_{CH_4 i}$, the total column
methane enhancement of the i-th plume ~~mask~~ pixel, and a_i, the area of this pixel.

Plume transport includes complicated three-dimensional and turbulent effects that require computer-intensive simulations to
be accounted for, if even possible given the randomness of turbulence. Through IME, the overall impacts of those effects are
presumably captured into a single effective wind speed, denoted U_{eff}. U_{eff} is calibrated against the 10-m wind speed provided
by meteorological models (U_{10m}) over a set of Large Eddy Simulations (LES) made for known synthetic emission rates, and
re-sampled according to a given instrument characteristics (spatial resolution, noise model, etc.). Thus, U_{eff} can be calibrated
for specific instruments and observing conditions. Varon et al. (2021) provide an effective wind speed calibration model for
Sentinel-2-like Earth imagers: $U_{\text{eff}} = 0.33 \times U_{10m} + 0.45$. ~~Using~~ This IME effective wind speed calibration slope which is lower
than 1 reflects the fact that the plume extent L, defined as the square root of the plume area, is smaller than the actual plume
length for long narrow plumes observed over land. This definition of L is chosen for its simplicity and because the plume
mask is ventilated by turbulent diffusion rather than uniform transport (Varon et al., 2018). Besides, using this effective wind
speed calibration implicitly assumes that the plume is observed in the same conditions as those used for the LES calibration,
including for instance that the full extent of the plume is visible as per the given instrument sensitivity.

2.3.2   Effective wind calibration of partial plume observation in IME

The IME method is critically sensitive to the plume mask extent. For a homogeneous plume of N pixels, the source rate
Q increases linearly with $\sqrt{N}$. In practice, the plume is not homogeneous and the number of pixels above the instrument
detection threshold relates to the emission rate, and truncating the plume mask because of external factors (low albedo, clouds,

etc.) biases Q. This IME sensitivity stems from the effective wind speed calibration that relies on an LES sampling of whole plume per the given instrument characteristics. Any systematic plume mask truncation therefore needs to be calibrated for. For the NS2 observation, only the small sea foam patch provides a high enough signal that could allow observation of part of the methane plume, above its source. This specific case therefore requires a custom effective wind calibration.

We consequently re-purpose an ensemble of LES simulations computed for a $275{\times}275$ m^2 source area (grossly the NS2 foam patch size) by Maasakkers et al. (2022), scale them to emission rates ranging from 100 to 1000 t/hr, re-sample them according to L8/S-2B instrumental characteristics and perform an effective wind speed calibration that only includes the pixels located above the source area in the plume mask. Following Varon et al. (2021), we perform a linear regression of U_{eff} against U_{10m} that is more appropriate for Sentinel-2-like instruments than the logarithm-based regression first proposed in Varon et al. (2018). We obtain the following NS2-custom effective wind speed calibration with an outlier-resilient Huber regression: $U_{\text{eff}} = 1.88 \times U_{\text{10m}} + 0.52$, with a standard deviation of data to fit mismatch values of 1.1 m/s (the Figure supporting this result is provided in the Supplements). This 1.88 calibration factor is significantly different from the slope value given in Sect. 2.3.1, applicable for ideal conditions over land. Its value higher than 1 reflects a different plume definition compared to ideal conditions over land, and must be interpreted as methane excess observed above the area source under-representing the actual emission rate of the full area source. Indeed, only the downwind plume integrates emissions from the all the area source, not the concentration field right above it. Actually, this IME effective wind speed calibration slope close to 2 is consistent with expectations from mass balance of a uniformly ventilated area source (wind direction above it is unique and not changing, a fair assumption at the scale of the NS2 leak) as shown by Buchwitz et al. (2017), and is significantly different from the slope value given in Sect. 2.3.1, applicable for ideal conditions over land.

2.4 ~~Ensemble~~ Monte Carlo ensemble approach for evaluating Nord Stream 2 leak rates as seen by Landsat 8 and Sentinel-2B

We use ~~an~~ a Monte Carlo ensemble approach to calculate the average methane leak rate from NS2, as seen by L8 and S-2B, using MBSP and IME with our custom calibrations. We ~~perturb~~ consider six different parameters that impact MBSP and/or IME results to generate ~~an~~ a Monte Carlo ensemble of leak rate quantifications:

(1) In MBSP, we ~~perturb the empirical calibration of the spectral dependence~~ use the distribution of sea foam albedo spectral dependence calibrations and randomly pick a calibration value from the satellite-wise sets of sea foam ~~albedo determined in~~ observations in ship trails described in Sect. 2.2.2 ~~by $\pm 1\sigma$ in 0.1σ steps.~~. By doing so, we implicitly follow the underlying distributions of each satellite-wise sea foam spectral dependence calibration values.

(2) To capture the uncertainty in the background, we estimate a non-enhanced methane background over the NS2 sea foam patch. It is computed by applying MBSP using a calibration coefficient exactly equal to the fitted s_1/s_2 ratio obtained from the NS2 sea foam pixels, thus ~~fully~~ compensating for possible methane enhancements. We then compute the standard deviation $\sigma_{X_{CH_4}}$ of this background signal, and use it to randomly shift the MBSP ~~enhancement results by $\pm 1\sigma_{X_{CH_4}}$ in $0.1\sigma_{X_{CH_4}}$ steps~~ background enhancement by sampling a Gaussian distribution with a standard deviation of $\sigma_{X_{CH_4}}$, and centred on zero.

(3) We ~~perturb~~ vary the plume mask extent by varying the minimum s_1 TOA reflectance value for a pixel to be included in the plume mask. These minimum s_1 TOA reflectance thresholds ~~cover~~ sample uniform distributions covering $[0, 0.07]$ for L8 and $[0, 0.045]$ for S-2B~~, with 0.005 steps for both satellites~~. We use different maximum thresholds for each satellite because the maximum TOA reflectance observed by L8 in the NS2 patch is higher than for S-2B (see Fig. 1).

(4) ~~We~~ Following Schuit et al. (2023), we include four different 10-m wind speeds to better account for wind speed uncertainty. Three come from meteorological re-analysis products: the European Centre for Medium-Range Weather Forecasts (ECMWF) ERA5 (Hersbach et al., 2020), the Global Forcasting System (GFS) from NOAA National Centers for Environmental Prediction (NCEP, 2000) and the Goddard Earth Observing System-Forward Processing (GESO-FP, Molod et al., 2012). Furthermore, we include the in-situ wind speed measured at Bornholm airport, which is located about 50 km away from the NS2 leak (IEM, 2023). For September 29th, we obtain wind speeds of 4.1, 6.6, 4.8 and 3.6 m/s from ERA5, GFS, GEOS-FP and airport measurements, respectively; and for September 30th, we obtain wind speeds of 5.0, 6.3, 6.3 and 5.7 m/s, respectively. We randomly pick one of these four wind speeds.

(5) ~~We perturb wind speed values by $\pm 50\%$, with 10% steps~~ To account for wind speed error, we evaluate the differences between the three re-analysis models (ERA5, GEOS-FP, GFS) and in-situ measurements made at Bornholm airport for 2022. On average, we find a standard deviation of 1.6 m/s. We therefore sample the wind speed error from a Gaussian distribution with a 1.6 m/s standard deviation and centred on zero.

(6) We ~~perturb~~ account for effective wind speed calibration ~~coefficients by $\pm 5\%$, with 1% steps~~ errors by randomly sampling data − fit mismatch values from the distribution shown in the Supplements (Figure S8). By doing so, we implicitly follow the slightly non-Gaussian skewed distribution that these mismatches show.

~~Overall, we get 3,201,660~~ We generate a Monte Carlo ensemble of 1,000,000 members for each satellite overpass, and ~~2,134,440 ensemble members for L8 and S-2B, respectively, and~~ report their averages, and standard deviations as uncertainty.

Besides these ensemble metrics, we also seek to determine which input parameters contribute most to the obtained ensemble variance. Thus, we also compute the first-order sensitivity indices S_i for our six parameters:

$$S_i = \frac{V_{X_i}\left(E_{\sim X_i}(Q|X_i)\right)}{V(Q)} \tag{3}$$

with X_i and $i \in \{1, 2, 3, 4, 5, 6\}$, the six parameters that we explore; Q, the leak rates that we compute; $E_{\sim X_i}$ the expectation across all parameters values but X_i that is fixed; V_{X_i}, the variance across all X_i values; and V, the usual variance. Citing Lo Piano et al. (2021), the plain language meaning of S_i is "the fractional reduction in the variance of Q which would be obtained on average if X_i could be fixed".

Here, we only rely on our single satellite-wise Monte Carlo ensembles and follow Lo Piano et al. (2021) to estimate S_i by directly calculating $V_{X_i}(E_{\sim X_i}(Q|X_i))$ as the variance of the smoothed Q against X_i scatter plot. As we randomly pick values from small sets for the sea foam albedo spectral dependence calibrations and wind speed products, we compute $E_{\sim X_i}(Q|X_i)$ for each discrete value that X_i can take. For wind speed and effective wind speed errors, as well as minimum albedo and methane enhancement shifts, where we sample continuous distributions, we use 1000 bins of 1000 ensemble members to smooth the Monte Carlo ensemble results.

3 Results and discussion: Nord Stream 2 leak rates

Figure 5 shows the distribution of leak rate values within the Monte Carlo ensembles for L8 and S-2B. We obtain ensemble-averaged methane leak rates of ~~433 ± 459~~ 507 ± 673 t/hr and ~~398 ± 449~~ 495 ± 640 t/hr for L8 and S-2B, respectively. ~~These ±1σ uncertainty intervals are mainly driven by the perturbation of the empirical calibration of~~ In addition, Table 1 provides the first-order sensitivity indices S_i corresponding to these uncertainties (the smoothed scatter plots supporting these indices are provided in the Supplements). From these indices, we conclude that the uncertainty of the sea foam albedo spectral dependence ~~(color scale in Fig. 5), and by the shift in the methane background. Leak~~ calibration mainly drives these Monte Carlo ensemble uncertainties. This is illustrated by the colour scale applied to the distributions included in Fig. 5: leak rates get lower and eventually negative with increasing empirical sea foam albedo spectral dependence calibration values.
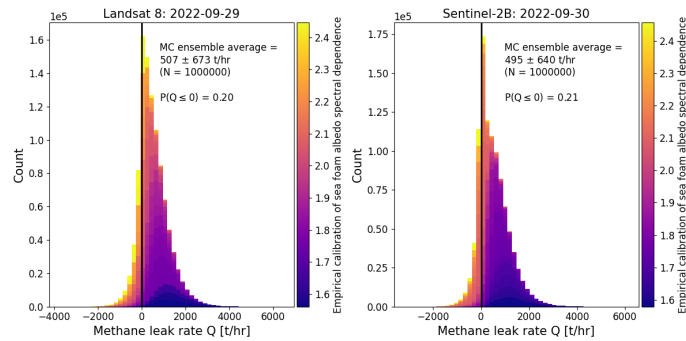
Figure 5. Distributions of methane emission rate values for the Landsat 8 (left) and Sentinel-2B (right) ensembles. ~~Ensemble~~ Monte Carlo ensemble means and standard deviations are shown inset, along with the fraction of null or negative emission rates, denoted as $P(Q \leq 0)$. The color scale shows the contributions of different sea foam albedo spectral dependence calibration values to the overall distribution of leak rates within the ensemble.

Input parameter	Landsat 8 S_i	Sentinel-2B S_i
Empirical calibration of sea foam albedo spectral dependence	0.52	0.62
Shift of methane background	0.18	0.12
Minimum albedo to include a pixel in the plume mask	0.02	0.03
Wind speed product	0.03	0.01
Wind speed error	0.06	0.04
Effective wind speed calibration error	0.01	0.01

Table 1. First-order sensitivity indices S_i, computed for each satellite observation and all six parameters included in our Monte Carlo ensembles.

The individual L8 and S-2B ensemble distributions have $\pm 1\sigma$ uncertainty intervals that include zero emissions, and show ~~$P(Q \leq 0) = 0.13$ and $P(Q \leq 0) = 0.12$~~ $P(Q \leq 0) = 0.20$ and $P(Q \leq 0) = 0.21$, respectively. ~~Consequently, considering these~~

~~null-hypothesis probabilities higher than 10%, no firm conclusion can be drawn regarding separate~~ These separate L8 and S-2B ~~detections of the~~ estimates may not be independent. For example, similar look-up-tables or IME effective wind calibration errors or biases may hamper them. However, if we opportunistically assume that they are, we can generate an ensemble representing the averaged combined L8 and S-2B NS2 ~~methane leak.~~ leak rate. We obtain an averaged L8 and S-2B NS2 methane leak rate of 501 ± 521 t/hr, with $P(Q \leq 0) = 0.12$. While these uncertainties are too large to draw firm conclusions, we note that both single and dual-overpass estimates show positive means and higher probabilities for positive Q values (79% − 88%) than negative ones (12% − 21%). This result hints that L8 and S-2B sensed a methane-related signal, which could be related to an emission magnitude of hundreds of tons per hour.

Because this NS2 observation case is singular and recent, very few results to compare to have been published. GHGSat reports leak rates of 79 t/hr and 29 t/hr for their NS2 glint observations made on Sept 30th (GHGSat, 2022). Jia et al. (2022) report no result for L8, and a methane leak rate of 72 ± 38 t/hr for S-2B, while also acknowledging significant uncertainties in their methodology regarding the spectral reflectance of bubbles and the partial imaging of the methane plume. The work performed here precisely describes the origin of the challenges posed by these specific NS2 observations, ~~and~~ addresses them through custom calibrations, and provides a comprehensive uncertainty analysis. All previously reported NS2 methane leak rates for September 30th are comprised within our large zero-including uncertainty range obtained for S-2B on that day.

~~If we opportunistically assume that the L8 and S-2B leak rate quantifications are independent (different satellites, but an identical method to process observations), we can generate an ensemble representing the averaged combined L8 and S-2B NS2 leak rate. Because distributions in Fig 5 are not Gaussian, we perform 100 random draws of 1M elements from the separate individual L8 and S-2B ensembles, from which we compute 1M element-wise averaged leak rates. On average, we obtain an averaged L8 and S-2B NS2 methane leak rate of 415 ± 321 t/hr, with $P(Q \leq 0) = 0.06$. Thus, under this favorable assumption, considering the null-hypothesis probability lower than 10%, these results give weak confidence that the dual-overpass combination of L8 and S-2B has indeed detected the NS2 methane leak.~~

4   Conclusions

We have evaluated the possibility of extracting methane emission information from Landsat 8 (L8) and Sentinel-2B (S-2B) observations of the Nord Stream 2 (NS2) pipeline leak.

We have shown how the unusual observations of a sea foam patch surrounded by dark still sea (and clouds for L8) challenge implicit underlying ~~hypotheses~~ assumptions in both the Multi-Band Single-Pass (MBSP) and Integrated Mass Enhancement (IME) methods. For MBSP, we showed that an external empirical calibration of the sea foam albedo spectral dependence is needed, and provided one by using sea foam observations in ship trails. This underlines how extreme surface heterogeneity can hamper the standard albedo spectral dependence calibration in MBSP. For IME, we showed that emission rate quantifications are critically sensitive to plume mask truncation, and we provided an effective wind speed calibration customized to the NS2 leak, ~~that is~~ for a plume only observed over a small sea foam patch. Plume masks over land can be truncated due to cloud

coverage or dark albedo artefacts (waterbodies like rivers, lakes, etc.), which then cause a similar emission rate underestimation.

Using these two-fold customized calibrations for MBSP and IME in ~~an~~ a Monte Carlo ensemble approach, we have assessed that no firm conclusion can be made about individual or combined L8 and S-2B detection of the NS2 methane leak. ~~If we opportunistically assume that they are independent, we obtain an averaged~~ Positive methane leak rates appear to be more likely than negative ones in both single and dual-overpass ~~(L8 and S-2B combined) NS2 methane leak rate of 415 ± 321~~ Monte Carlo ensemble estimates, and point towards a best estimate of 501 ± 521 t/hr~~, with only a small null-hypothesis probability $P(Q \leq 0) = 0.06$~~.

~~Our work illustrates~~ Overall, we see our work as a methodological cautionary tale illustrating how implicit method ~~hypotheses~~ assumptions need to be considered and compensated for in unusual observation cases such as this one. Our nuanced results with large uncertainties are not surprising: this exceptional Nord Stream leak event pushed Earth imagers that were not initially designed to observe greenhouse gases - even less over water - to their very limits.

Data availability. Landsat 8 and Sentinel-2B data used in this work are publicly available and were retrieved from the Google Earth Engine as 2 km-side square images of given targets, from collections `LANDSAT/LC08/C02/T1_TOA` and `COPERNICUS/S2_HARMONIZED`, respectively. All images are listed in the Supplements.

Author contributions. MD and JDM conceived the study. MD performed the satellite data analysis and emission rate quantifications, with supervision from JDM and IA. DJV performed the tailored Nord Stream 2 effective wind speed calibration. MD wrote this article with feedback from all co-authors.

Competing interests. The authors have the following competing interests: At least one of the (co-)authors is a member of the editorial board of Atmospheric Measurement Techniques.

Acknowledgements. This work is in part supported through the ESA funded MethaneCamp project. Copernicus (modified) Sentinel-2 data (2022) have been used. Authors are grateful to Itziar Irakulis-Loitxate and Otto Hasekamp for the helpful discussions and comments while designing this work. The authors are also grateful to the two referees whose comments helped improve this work.

References

Buchwitz, M., Schneising, O., Reuter, M., Heymann, J., Krautwurst, S., Bovensmann, H., Burrows, J. P., Boesch, H., Parker, R. J., Somkuti, P., Detmers, R. G., Hasekamp, O. P., Aben, I., Butz, A., Frankenberg, C., and Turner, A. J.: Satellite-derived methane hotspot emission estimates using a fast data-driven method, Atmospheric Chemistry and Physics, 17, 5751–5774, https://doi.org/10.5194/acp-17-5751-2017, 2017.

Drusch, M., Del Bello, U., Carlier, S., Colin, O., Fernandez, V., Gascon, F., Hoersch, B., Isola, C., Laberinti, P., Martimort, P., Meygret, A., Spoto, F., Sy, O., Marchese, F., and Bargellini, P.: Sentinel-2: ESA's Optical High-Resolution Mission for GMES Operational Services, Remote Sensing of Environment, 120, 25–36, https://doi.org/https://doi.org/10.1016/j.rse.2011.11.026, the Sentinel Missions - New Opportunities for Science, 2012.

Frankenberg, C., Thorpe, A. K., Thompson, D. R., Hulley, G., Kort, E. A., Vance, N., Borchardt, J., Krings, T., Gerilowski, K., Sweeney, C., Conley, S., Bue, B. D., Aubrey, A. D., Hook, S., and Green, R. O.: Airborne methane remote measurements reveal heavy-tail flux distribution in Four Corners region, Proceedings of the National Academy of Sciences, 113, 9734–9739, https://doi.org/10.1073/pnas.1605617113, 2016.

GHGSat: GHGSat measures its largest emission from a single source ever from Nord Stream 2 leak, https://www.ghgsat.com/en/newsroom/ghgsat-nordstream/, accessed: 2023-05-10, 2022.

Gordon, I., Rothman, L., Hargreaves, R., Hashemi, R., Karlovets, E., Skinner, F., Conway, E., Hill, C., Kochanov, R., Tan, Y., Wcisło, P., Finenko, A., Nelson, K., Bernath, P., Birk, M., Boudon, V., Campargue, A., Chance, K., Coustenis, A., Drouin, B., Flaud, J., Gamache, R., Hodges, J., Jacquemart, D., Mlawer, E., Nikitin, A., Perevalov, V., Rotger, M., Tennyson, J., Toon, G., Tran, H., Tyuterev, V., Adkins, E., Baker, A., Barbe, A., Canè, E., Császár, A., Dudaryonok, A., Egorov, O., Fleisher, A., Fleurbaey, H., Foltynowicz, A., Furtenbacher, T., Harrison, J., Hartmann, J., Horneman, V., Huang, X., Karman, T., Karns, J., Kassi, S., Kleiner, I., Kofman, V., Kwabia–Tchana, F., Lavrentieva, N., Lee, T., Long, D., Lukashevskaya, A., Lyulin, O., Makhnev, V., Matt, W., Massie, S., Melosso, M., Mikhailenko, S., Mondelain, D., Müller, H., Naumenko, O., Perrin, A., Polyansky, O., Raddaoui, E., Raston, P., Reed, Z., Rey, M., Richard, C., Tóbiás, R., Sadiek, I., Schwenke, D., Starikova, E., Sung, K., Tamassia, F., Tashkun, S., Vander Auwera, J., Vasilenko, I., Vigasin, A., Villanueva, G., Vispoel, B., Wagner, G., Yachmenev, A., and Yurchenko, S.: The HITRAN2020 molecular spectroscopic database, Journal of Quantitative Spectroscopy and Radiative Transfer, 277, 107 949, https://doi.org/https://doi.org/10.1016/j.jqsrt.2021.107949, 2022.

Hersbach, H., Bell, B., Berrisford, P., Hirahara, S., Horányi, A., Muñoz-Sabater, J., Nicolas, J., Peubey, C., Radu, R., Schepers, D., Simmons, A., Soci, C., Abdalla, S., Abellan, X., Balsamo, G., Bechtold, P., Biavati, G., Bidlot, J., Bonavita, M., De Chiara, G., Dahlgren, P., Dee, D., Diamantakis, M., Dragani, R., Flemming, J., Forbes, R., Fuentes, M., Geer, A., Haimberger, L., Healy, S., Hogan, R. J., Hólm, E., Janisková, M., Keeley, S., Laloyaux, P., Lopez, P., Lupu, C., Radnoti, G., de Rosnay, P., Rozum, I., Vamborg, F., Villaume, S., and Thépaut, J.-N.: The ERA5 global reanalysis, Quarterly Journal of the Royal Meteorological Society, 146, 1999–2049, https://doi.org/https://doi.org/10.1002/qj.3803, 2020.

IEM: ASOS-AWOS-METAR Data Download, Iowa Environmental Mesonet (IEM), https://mesonet.agron.iastate.edu/ASOS/, accessed: 2023-05-09, 2023.

IMEO: Satellite detects methane plume in Nord Stream leak, https://twitter.com/MethaneData/status/1575610350548164608, accessed: 2023-07-20, 2022.

IPCC: Summary for Policymakers, pp. 3–32, Cambridge University Press, Cambridge, United Kingdom and New York, NY, USA, https://doi.org/10.1017/9781009157896.001, 2021.

Irakulis-Loitxate, I., Gorroño, J., Zavala-Araiza, D., and Guanter, L.: Satellites Detect a Methane Ultra-emission Event from an Offshore Platform in the Gulf of Mexico, Environmental Science & Technology Letters, 9, 520–525, https://doi.org/10.1021/acs.estlett.2c00225, 2022a.

Irakulis-Loitxate, I., Guanter, L., Maasakkers, J. D., Zavala-Araiza, D., and Aben, I.: Satellites Detect Abatable Super-Emissions in One of the World's Largest Methane Hotspot Regions, Environmental Science & Technology, 56, 2143–2152, https://doi.org/10.1021/acs.est.1c04873, pMID: 35102741, 2022b.

Jervis, D., McKeever, J., Durak, B. O. A., Sloan, J. J., Gains, D., Varon, D. J., Ramier, A., Strupler, M., and Tarrant, E.: The GHGSat-D imaging spectrometer, Atmospheric Measurement Techniques, 14, 2127–2140, https://doi.org/10.5194/amt-14-2127-2021, 2021.

Jia, M., Li, F., Zhang, Y., Wu, M., Li, Y., Feng, S., Wang, H., Chen, H., Ju, W., Lin, J., Cai, J., Zhang, Y., and Jiang, F.: The Nord Stream pipeline gas leaks released approximately 220,000 tonnes of methane into the atmosphere, Environmental Science and Ecotechnology, 12, 100 210, https://doi.org/https://doi.org/10.1016/j.ese.2022.100210, 2022.

Koepke, P.: Effective reflectance of oceanic whitecaps, Appl. Opt., 23, 1816–1824, https://doi.org/10.1364/AO.23.001816, 1984.

Lauvaux, T., Giron, C., Mazzolini, M., d'Aspremont, A., Duren, R., Cusworth, D., Shindell, D., and Ciais, P.: Global assessment of oil and gas methane ultra-emitters, Science, 375, 557–561, https://doi.org/10.1126/science.abj4351, 2022.

Lo Piano, S., Ferretti, F., Puy, A., Albrecht, D., and Saltelli, A.: Variance-based sensitivity analysis: The quest for better estimators and designs between explorativity and economy, Reliability Engineering & System Safety, 206, 107 300, https://doi.org/https://doi.org/10.1016/j.ress.2020.107300, 2021.

Lorente, A., Borsdorff, T., Butz, A., Hasekamp, O., aan de Brugh, J., Schneider, A., Wu, L., Hase, F., Kivi, R., Wunch, D., Pollard, D. F., Shiomi, K., Deutscher, N. M., Velazco, V. A., Roehl, C. M., Wennberg, P. O., Warneke, T., and Landgraf, J.: Methane retrieved from TROPOMI: improvement of the data product and validation of the first 2 years of measurements, Atmospheric Measurement Techniques, 14, 665–684, https://doi.org/10.5194/amt-14-665-2021, 2021.

Maasakkers, J. D., Varon, D. J., Elfarsdóttir, A., McKeever, J., Jervis, D., Mahapatra, G., Pandey, S., Lorente, A., Borsdorff, T., Foorthuis, L. R., Schuit, B. J., Tol, P., van Kempen, T. A., van Hees, R., and Aben, I.: Using satellites to uncover large methane emissions from landfills, Science Advances, 8, eabn9683, https://doi.org/10.1126/sciadv.abn9683, 2022.

Molod, A., Takacs, L., Suarez, M., Bacmeister, J., Song, I.-S., and Eichmann, A.: The GEOS-5 Atmospheric General Circulation Model: Mean Climate and Development from MERRA to Fortuna, Tech. rep., NASA, https://ntrs.nasa.gov/citations/20120011790, 2012.

NCEP: NCEP FNL Operational Model Global Tropospheric Analyses, Tech. rep., https://doi.org/https://doi.org/10.5065/D6M043C6, 2000.

Nisbet, E. G., Fisher, R. E., Lowry, D., France, J. L., Allen, G., Bakkaloglu, S., Broderick, T. J., Cain, M., Coleman, M., Fernandez, J., Forster, G., Griffiths, P. T., Iverach, C. P., Kelly, B. F. J., Manning, M. R., Nisbet-Jones, P. B. R., Pyle, J. A., Townsend-Small, A., al Shalaan, A., Warwick, N., and Zazzeri, G.: Methane Mitigation: Methods to Reduce Emissions, on the Path to the Paris Agreement, Reviews of Geophysics, 58, e2019RG000 675, https://doi.org/https://doi.org/10.1029/2019RG000675, e2019RG000675 2019RG000675, 2020.

Pandey, S., Gautam, R., Houweling, S., van der Gon, H. D., Sadavarte, P., Borsdorff, T., Hasekamp, O., Landgraf, J., Tol, P., van Kempen, T., Hoogeveen, R., van Hees, R., Hamburg, S. P., Maasakkers, J. D., and Aben, I.: Satellite observations reveal extreme methane leakage from a natural gas well blowout, Proceedings of the National Academy of Sciences, 116, 26 376–26 381, https://doi.org/10.1073/pnas.1908712116, 2019.

Roy, D., Wulder, M., Loveland, T., C.E., W., Allen, R., Anderson, M., Helder, D., Irons, J., Johnson, D., Kennedy, R., Scambos, T., Schaaf, C., Schott, J., Sheng, Y., Vermote, E., Belward, A., Bindschadler, R., Cohen, W., Gao, F., Hipple, J., Hostert, P., Huntington, J., Justice, C., Kilic, A., Kovalskyy, V., Lee, Z., Lymburner, L., Masek, J., McCorkel, J., Shuai, Y., Trezza, R., Vogelmann, J., Wynne, R., and

Zhu, Z.: Landsat-8: Science and product vision for terrestrial global change research, Remote Sensing of Environment, 145, 154–172, https://doi.org/https://doi.org/10.1016/j.rse.2014.02.001, 2014.

Sanderson, K.: What do Nord Stream methane leaks mean for climate change?, https://doi.org/https://doi.org/10.1038/d41586-022-03111-x, accessed: 2023-05-10, 2022.

Schuit, B. J., Maasakkers, J. D., Bijl, P., Mahapatra, G., Van den Berg, A.-W., Pandey, S., Lorente, A., Borsdorff, T., Houweling, S., Varon, D. J., McKeever, J., Jervis, D., Girard, M., Irakulis-Loitxate, I., Gorroño, J., Guanter, L., Cusworth, D. H., and Aben, I.: Automated detection and monitoring of methane super-emitters using satellite data, Atmospheric Chemistry and Physics Discussions, 2023, 1–47, https://doi.org/10.5194/acp-2022-862, 2023.

Sentinel-Hub: EO Browser, https://apps.sentinel-hub.com/eo-browser, accessed: 2023-07-21, 2023.

Varon, D. J., Jacob, D. J., McKeever, J., Jervis, D., Durak, B. O. A., Xia, Y., and Huang, Y.: Quantifying methane point sources from fine-scale satellite observations of atmospheric methane plumes, Atmospheric Measurement Techniques, 11, 5673–5686, https://doi.org/10.5194/amt-11-5673-2018, 2018.

Varon, D. J., Jervis, D., McKeever, J., Spence, I., Gains, D., and Jacob, D. J.: High-frequency monitoring of anomalous methane point sources with multispectral Sentinel-2 satellite observations, Atmospheric Measurement Techniques, 14, 2771–2785, https://doi.org/10.5194/amt-14-2771-2021, 2021.

Veefkind, J., Aben, I., McMullan, K., Förster, H., de Vries, J., Otter, G., Claas, J., Eskes, H., de Haan, J., Kleipool, Q., van Weele, M., Hasekamp, O., Hoogeveen, R., Landgraf, J., Snel, R., Tol, P., Ingmann, P., Voors, R., Kruizinga, B., Vink, R., Visser, H., and Levelt, P.: TROPOMI on the ESA Sentinel-5 Precursor: A GMES mission for global observations of the atmospheric composition for climate, air quality and ozone layer applications, Remote Sensing of Environment, 120, 70–83, https://doi.org/https://doi.org/10.1016/j.rse.2011.09.027, the Sentinel Missions - New Opportunities for Science, 2012.

Whitlock, C. H., Bartlett, D. S., and Gurganus, E. A.: Sea foam reflectance and influence on optimum wavelength for remote sensing of ocean aerosols, Geophysical Research Letters, 9, 719–722, https://doi.org/https://doi.org/10.1029/GL009i006p00719, 1982.

Supplements to:

Report on Landsat 8 and Sentinel-2B observations of the Nord Stream 2 pipeline methane leak

Matthieu Dogniaux[1], Joannes D. Maasakkers[1], Daniel J. Varon[2] and Ilse Aben[1]

[1]SRON Netherlands Institute for Space Research, Leiden, The Netherlands

[2]School of Engineering and Applied Science, Harvard University, Cambridge, USA

Corresponding author: Matthieu Dogniaux

Email: M.Dogniaux@sron.nl

Tables S1, S2 and S3 list all the 2-km-side satellite images used in this work. Figures S1 to S7 show all individual fits for sea foam observations in boat trails. Figure S8 shows the effective wind calibration dataset, and Figures S9 and S10 support the calculation of first-order sensitivity indices.

430

Table S1: Nord Stream 2 (NS2) leak satellite images used in this work

Satellite	date	Latitude	Longitude	Filters
Landsat 8	2022-09-29	54.877	15.409	Still sea:
				$s_2 < 0.04$ and $s_1 \leq 1.65\ s_2$
				Clouds: $s_2 \geq 0.04$
				NS2 sea foam:
				$s_2 < 0.04$ and $s_1 > 1.65\ s_2$
Sentinel-2B	2022-09-30	54.877	15.409	Still sea: $s_1 \leq 0.0045$
				NS2 sea foam: $s_1 > 0.0045$
				No cloud filtering required for this S-2B image

Table S2: Landsat 8 ship trail images used in this work

#	Satellite	date	Latitude	Longitude	τ_1	τ_2	c_i
1	Landsat 8	2022-09-02	55.972	11.196	0.0075	0.0400	1.92
2	Landsat 8	2022-09-02	54.598	11.305	0.0050	0.0300	1.86
3	Landsat 8	2022-09-02	54.268	11.699	0.0050	0.0250	1.64
4	Landsat 8	2022-09-06	58.814	18.071	0.0050	0.0300	1.75
5	Landsat 8	2022-09-10	59.847	25.522	0.0035	0.0250	1.58
6	Landsat 8	2022-09-11	~~54.527~~ 54.537	~~12.245~~ 12.220	~~0.0040~~ 0.0035	~~0.0400~~ 0.0200	1.80
7	Landsat 8	2022-09-11	~~54.537~~ 54.527	~~12.220~~ 12.245	~~0.0035~~ 0.0040	~~0.0200~~ 0.0400	1.56
8	Landsat 8	2022-09-16	57.619	9.834	0.0080	0.0600	2.19
9	Landsat 8	2022-09-16	57.627	9.851	0.0070	0.0250	1.89
10	Landsat 8	2022-09-16	57.634	9.897	0.0080	0.0300	2.05
11	Landsat 8	2022-09-16	57.682	9.814	0.0085	0.0300	1.76
12	Landsat 8	2022-09-16	56.734	7.976	0.0080	0.0300	2.22
13	Landsat 8	2022-09-25	57.122	10.760	0.0055	0.0300	1.98
14	Landsat 8	2022-09-25	54.131	8.013	0.0065	0.0150	2.43
15	Landsat 8	2022-10-02	~~57.574~~ 57.611	~~8.855~~ 9.921	~~0.0075~~ 0.0080	~~0.0200~~ 0.0250	1.99
16	Landsat 8	2022-10-02	57.721	8.481	0.0055	0.0200	2.04
17	Landsat 8	2022-10-02	~~57.611~~ 57.574	~~9.921~~ 8.855	~~0.0080~~ 0.0075	~~0.0250~~ 0.0200	2.25
18	Landsat 8	2022-10-02	57.563	8.884	0.0065	0.0300	1.76
19	Landsat 8	2022-10-04	54.461	10.261	0.0080	0.0150	2.10
20	Landsat 8	2022-10-06	63.508	20.536	0.0065	0.0300	2.05
21	Landsat 8	2022-10-06	54.878	13.070	0.0100	0.0300	1.79
22	Landsat 8	2022-10-10	58.846	21.509	0.0070	0.0300	1.83
23	Landsat 8	2022-10-15	56.613	17.809	0.0115	0.0300	1.88
24	Landsat 8	2022-10-18	57.614	9.918	0.0105	0.0300	2.25
25	Landsat 8	2022-10-18	57.674	9.774	0.0100	0.0500	2.45

Table S2: Landsat 8 ship trail images used in this work (Continued)

#	Satellite	date	Latitude	Longitude	τ_1	τ_2	c_i
26	Landsat 8	2022-10-20	55.957	11.260	0.0250	0.0350	2.09
27	Landsat 8	2022-10-20	55.169	12.888	0.0070	0.0200	1.79

Table S3: Sentinel-2B ship trail images used in this work

#	Satellite	date	Latitude	Longitude	τ_1	τ_2	c_i
1	Sentinel-2B	2022-09-02	~~56.700~~ 56.748	~~7.823~~ 7.958	0.0040	0.0400	1.75
2	Sentinel-2B	2022-09-02	~~56.748~~ 56.700	~~7.958~~ 7.823	0.0040	0.0400	1.91
3	Sentinel-2B	2022-09-03	54.369	11.981	0.0050	0.0400	1.64
4	Sentinel-2B	2022-09-03	54.390	11.992	0.0050	0.0400	1.85
5	Sentinel-2B	2022-09-06	56.851	11.812	0.0080	0.0600	1.67
6	Sentinel-2B	2022-09-06	56.856	11.840	0.0090	0.0300	1.77
7	Sentinel-2B	2022-09-06	57.456	11.453	0.0070	0.0300	1.85
8	Sentinel-2B	2022-09-07	54.574	18.878	0.0045	0.0400	1.69
9	Sentinel-2B	2022-09-09	55.789	10.741	0.0115	0.0350	1.77
10	Sentinel-2B	2022-09-13	~~54.315~~ 54.530	~~11.833~~ 11.427	~~0.0070~~ 0.0090	~~0.0400~~ 0.0200	1.67
11	Sentinel-2B	2022-09-13	54.541	11.410	0.0080	0.0150	1.63
12	Sentinel-2B	2022-09-13	~~54.530~~ 54.315	~~11.427~~ 11.833	~~0.0090~~ 0.0070	~~0.0200~~ 0.0400	1.80
13	Sentinel-2B	2022-09-16	56.032	10.737	0.0200	0.0375	2.46
14	Sentinel-2B	2022-09-19	57.676	9.673	0.0070	0.0400	1.95
15	Sentinel-2B	2022-09-19	57.464	10.935	0.0120	0.0300	2.04
16	Sentinel-2B	2022-09-19	57.472	8.615	0.0045	0.0500	1.76
17	Sentinel-2B	2022-09-30	54.982	18.303	0.0050	0.0500	1.97
18	Sentinel-2B	2022-09-30	54.876	17.373	0.0040	0.0350	1.59
19	Sentinel-2B	2022-09-30	54.830	13.773	0.0070	0.0300	2.09
20	Sentinel-2B	2022-09-30	54.304	13.980	0.0060	0.0400	1.82
21	Sentinel-2B	2022-10-02	57.681	9.873	0.0160	0.0350	2.22
22	Sentinel-2B	2022-10-02	57.794	9.230	0.0070	0.0410	2.12
23	Sentinel-2B	2022-10-03	54.613	11.309	0.0115	0.0400	2.09
24	Sentinel-2B	2022-10-03	54.629	11.311	0.0100	0.0500	2.07
25	Sentinel-2B	2022-10-06	54.448	12.055	0.0110	0.0400	1.58

#	Satellite	date	Latitude	Longitude	τ_1	τ_2	c_i
26	Sentinel-2B	2022-10-06	54.442	12.008	0.0110	0.0400	1.69
27	Sentinel-2B	2022-10-07	54.880	19.232	0.0110	0.0200	1.76
28	Sentinel-2B	2022-10-10	55.528	15.159	0.0110	0.0300	1.82
29	Sentinel-2B	2022-10-12	57.679	9.650	0.0110	0.0400	2.10
30	Sentinel-2B	2022-10-12	57.621	9.932	0.0080	0.0400	2.09
31	Sentinel-2B	2022-10-16	54.292	12.024	0.0070	0.0300	1.72
32	Sentinel-2B	2022-10-16	~~54.580~~ 54.568	~~11.277~~ 11.278	~~0.0090~~ 0.0105	~~0.0300~~ 0.0400	2.31
33	Sentinel-2B	2022-10-16	~~54.568~~ 54.580	~~11.278~~ 11.277	~~0.0105~~ 0.0090	~~0.0400~~ 0.0300	2.16
34	Sentinel-2B	2022-10-19	~~57.788~~ 57.673	~~10.140~~ 9.715	~~0.0050~~ 0.0045	0.0300	2.19
35	Sentinel-2B	2022-10-19	~~57.673~~ 57.788	~~9.715~~ 10.140	~~0.0045~~ 0.0050	0.0300	2.13
36	Sentinel-2B	2022-10-20	54.800	13.774	0.0200	0.0300	2.16
37	Sentinel-2B	2022-10-30	56.678	17.251	0.0070	0.0400	1.75
38	Sentinel-2B	2022-10-30	55.284	14.162	0.0210	0.0400	1.81
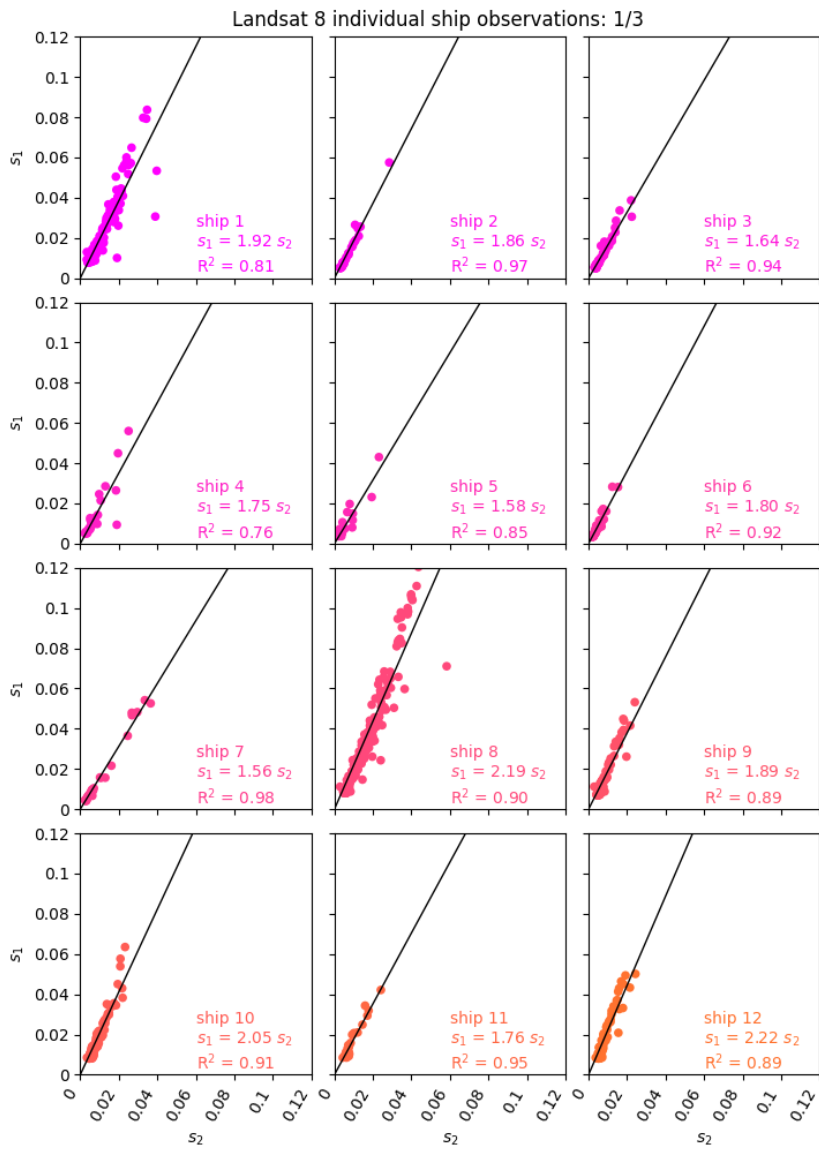
Figure S1. Individual Landsat 8 sea foam observations in ship trails and least-squares linear regression lines with intercepts forced to zero (1/3).
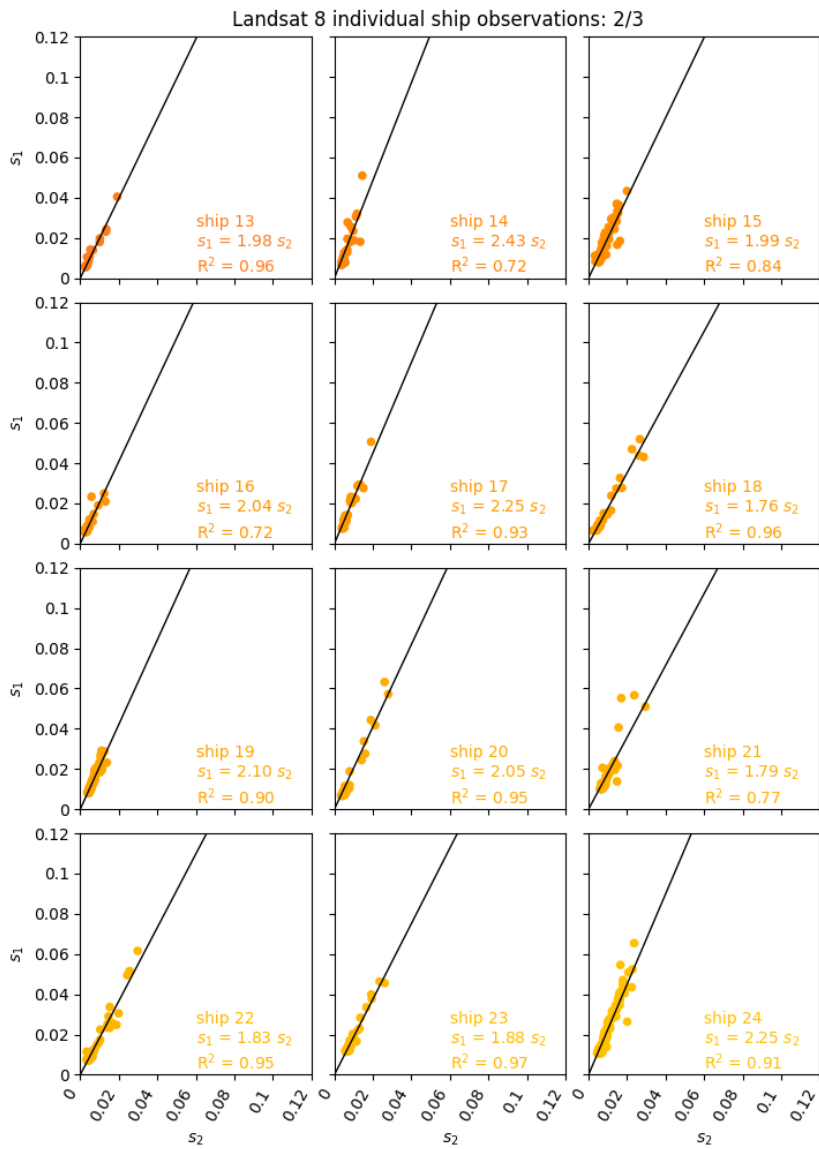
Figure S2. Individual Landsat 8 sea foam observations in ship trails and least-squares linear regression lines with intercepts forced to zero (2/3).
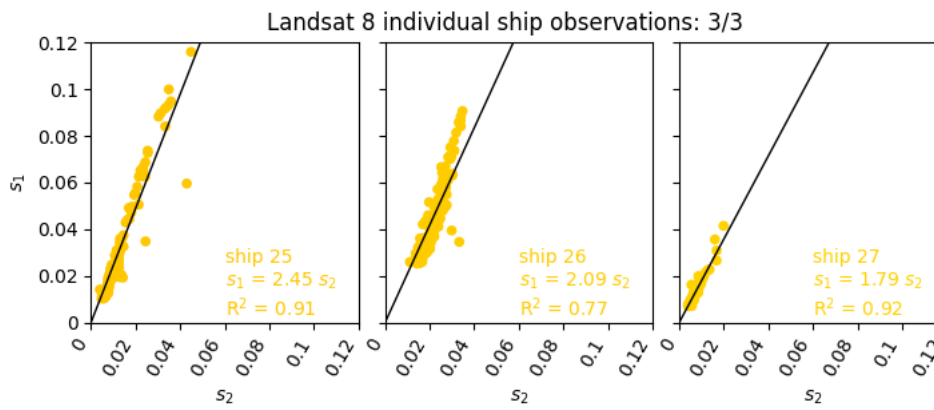
Figure S3. Individual Landsat 8 sea foam observations in ship trails and least-squares linear regression lines with intercepts forced to zero (3/3).
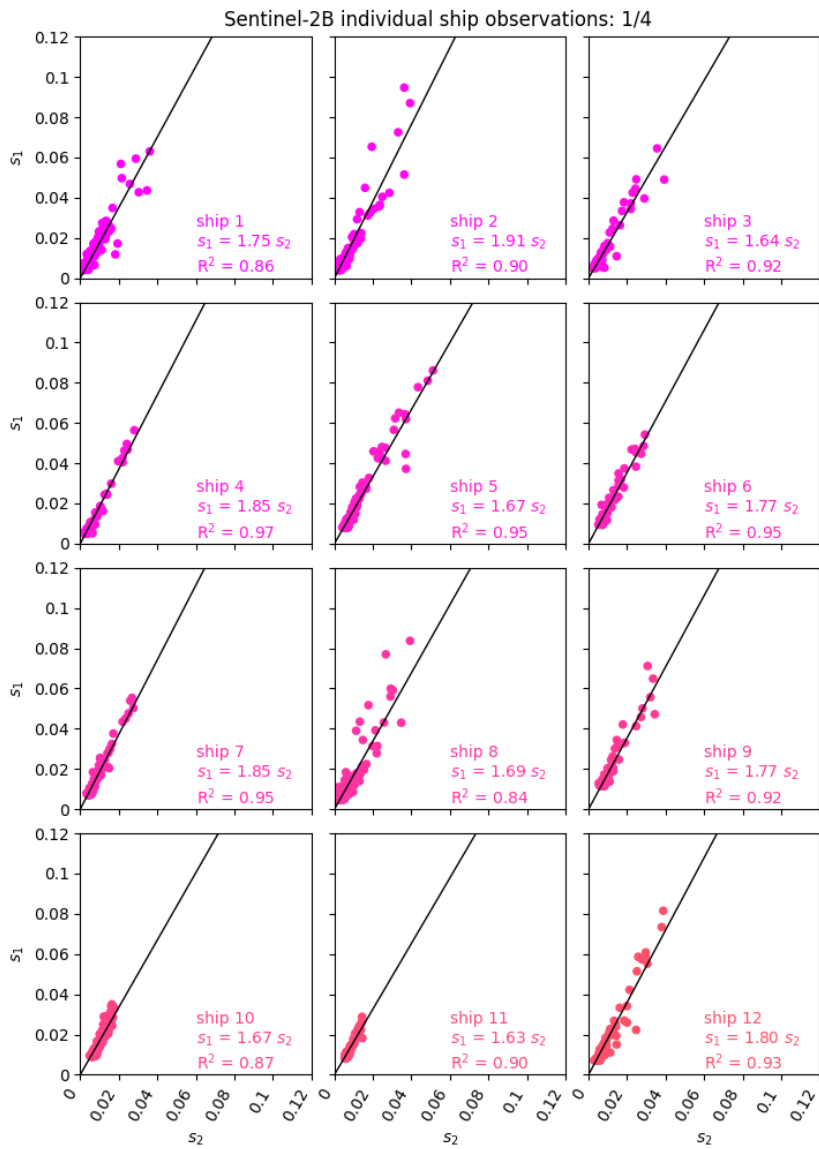
Figure S4. Individual Sentinel-2B sea foam observations in ship trails and least-squares linear regression lines with intercepts forced to zero (1/4).
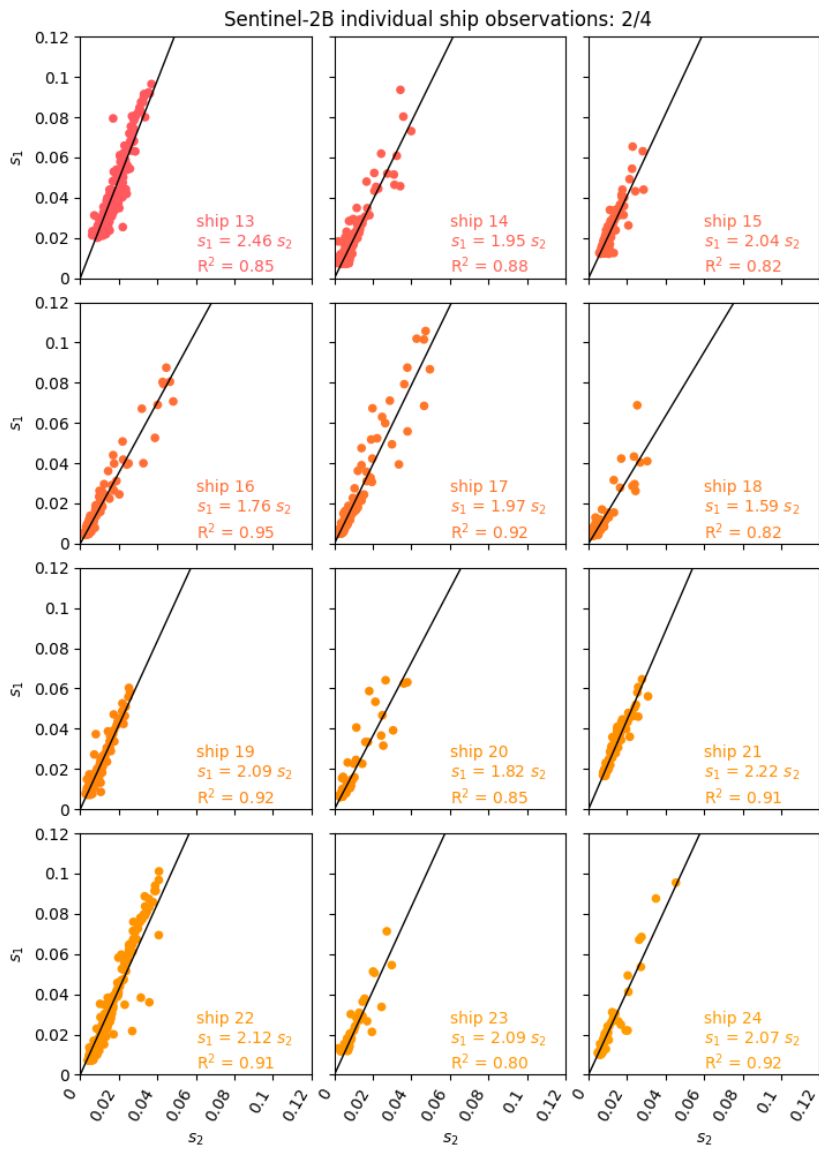
Figure S5. Individual Sentinel-2B sea foam observations in ship trails and least-squares linear regression lines with intercepts forced to zero (2/4).
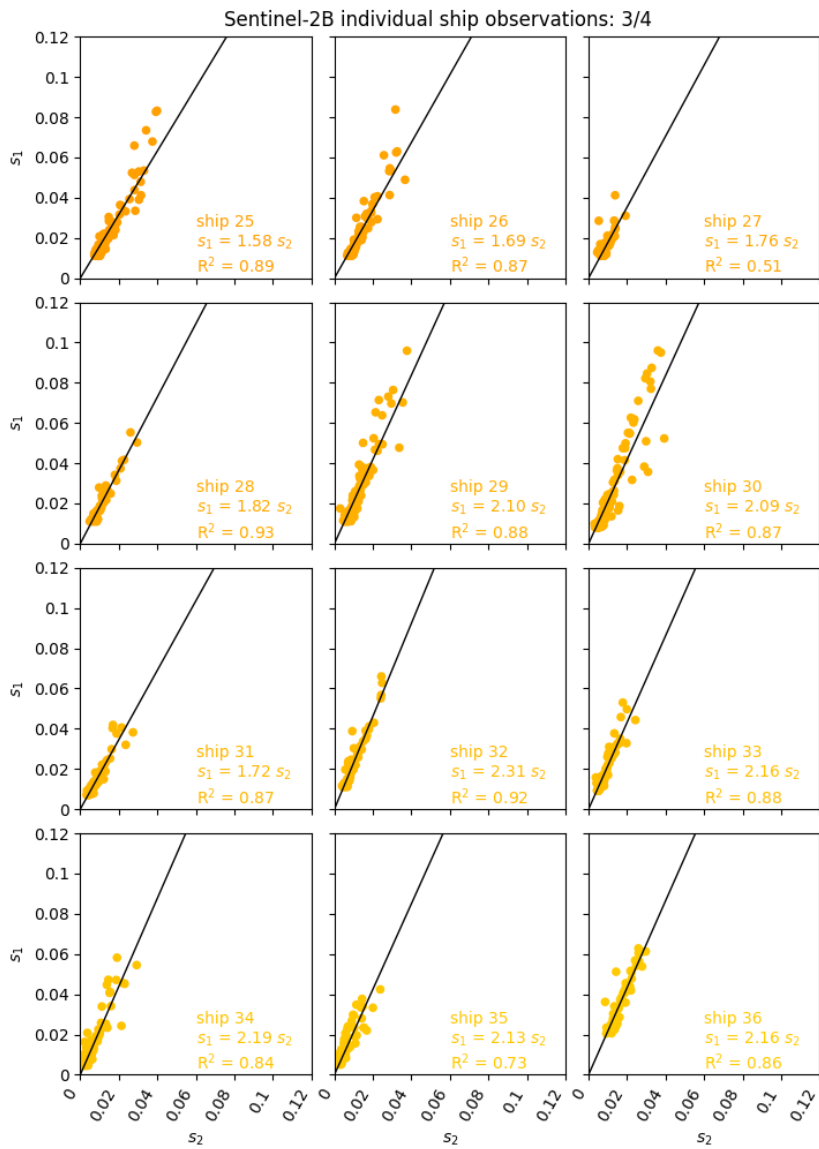
Figure S6. Individual Sentinel-2B sea foam observations in ship trails and least-squares linear regression lines with intercepts forced to zero (3/4).
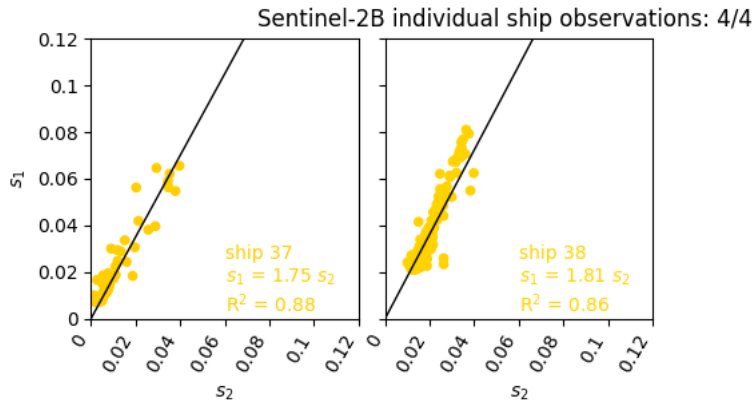
Figure S7. Individual Sentinel-2B sea foam observations in ship trails and least-squares linear regression lines with intercepts forced to zero (4/4).
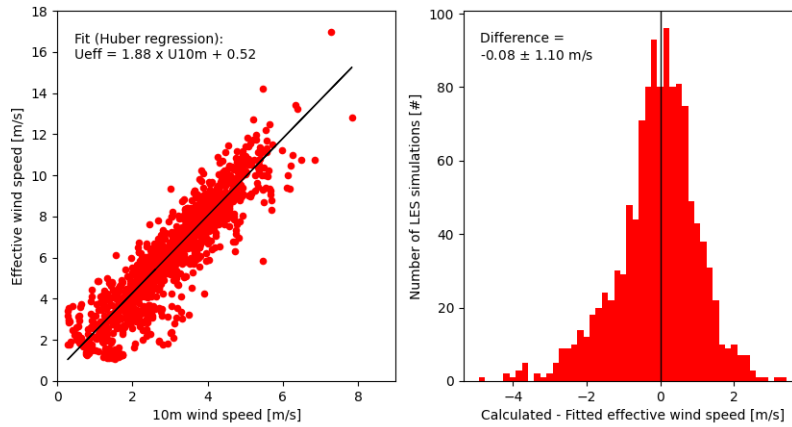
Figure S8. Calibration of IME effective wind speed against 10-m wind speed on the set of Large Eddy Simulation (LES) outputs from Maasakkers et al. (2022) for a 275×275 m^2 source area and sampled only over that same area (left). The distribution of calculated − fitted mismatches used in the Monte Carlo ensembles of Sect. 2.4 is given as well (right).
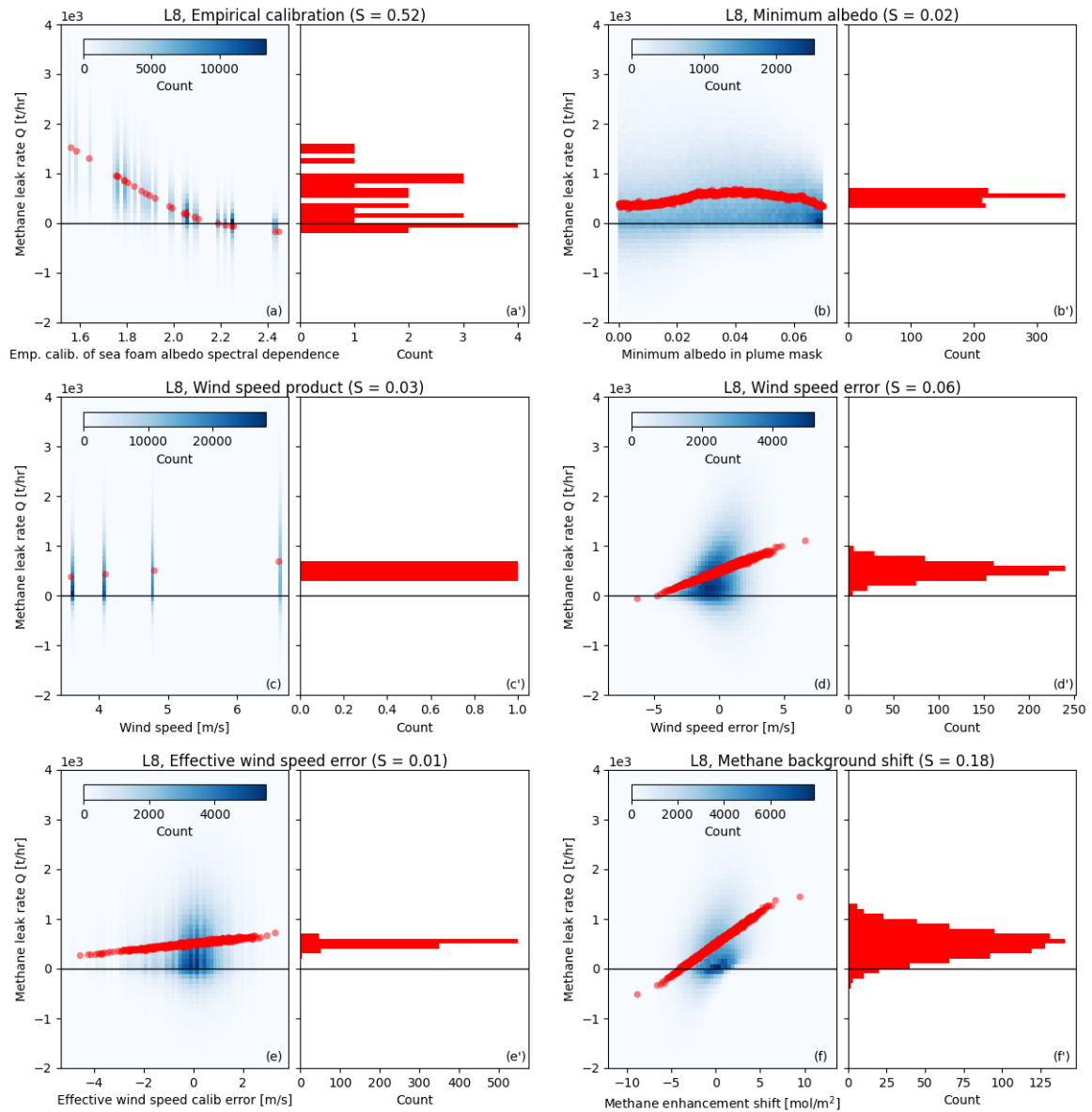
Figure S9. Two-dimensional histograms of Monte Carlo ensemble members showing the computed Landsat 8 methane leak rate Q against: (a) the empirical sea foam albedo spectral dependence, (b) the minimum albedo for pixels to be considered in the plume mask, (c) the wind speed product choice, (d) the wind speed error, (e) the effective wind speed calibration error, and (f) the methane background shift. Smoothed methane leak rate results $E_{\sim X_i}(Q|X_i)$ are shown for all parameters with red points, and their respective distributions are shown in panels next to the two-dimensional histograms (a',b',c',d',e' and f', respectively). Titles include satellite and parameter names, along with the first-order sensitivity index S associated to each parameter.
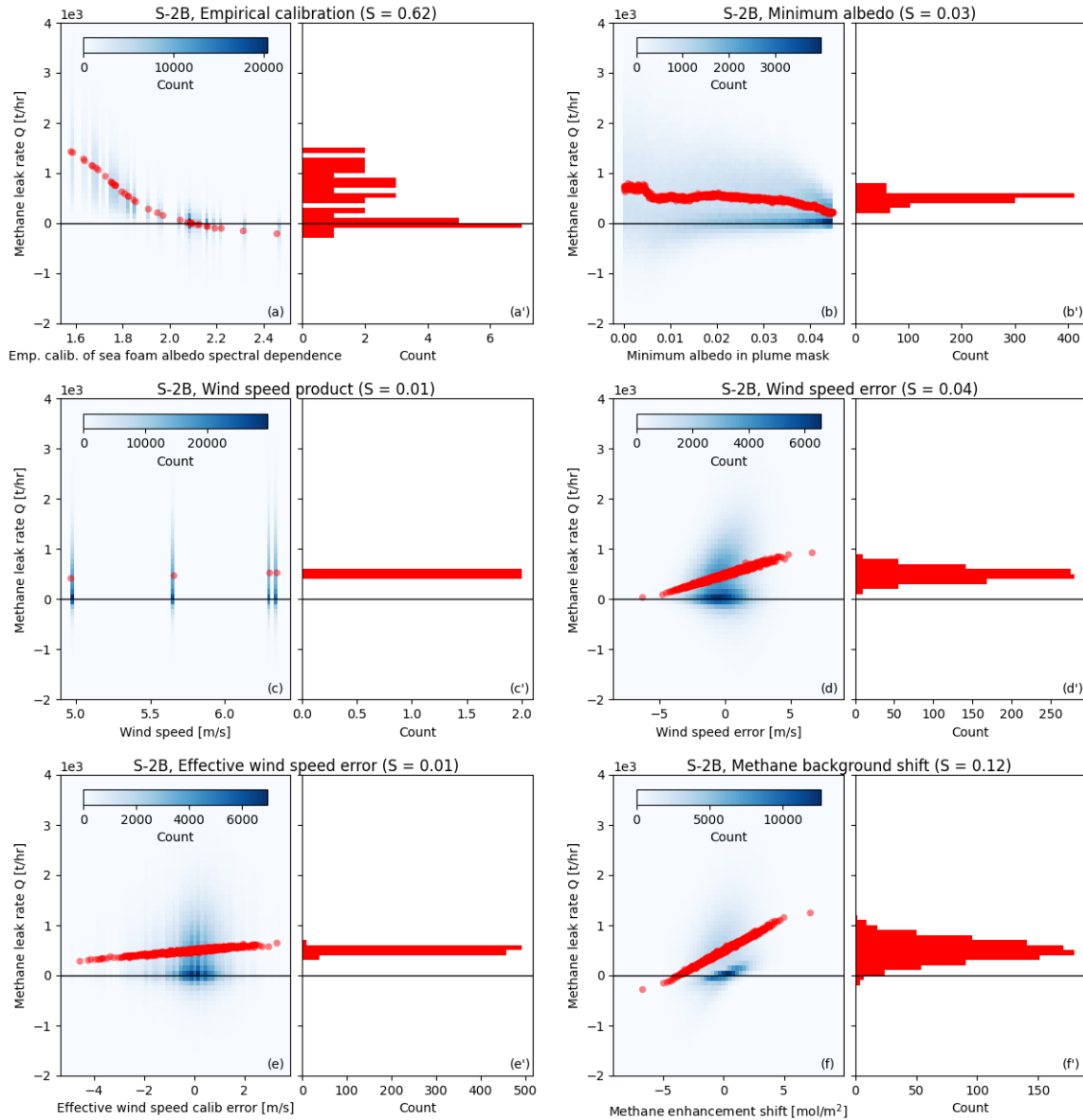
Figure S10. Two-dimensional histograms of Monte Carlo ensemble members showing the computed Sentinel-2B methane leak rate Q against: (a) the empirical sea foam albedo spectral dependence, (b) the minimum albedo for pixels to be considered in the plume mask, (c) the wind speed product choice, (d) the wind speed error, (e) the effective wind speed calibration error, and (f) the methane background shift. Smoothed methane leak rate results $E_{\sim X_i}(Q|X_i)$ are shown for all parameters with red points, and their respective distributions are shown in panels next to the two-dimensional histograms (a',b',c',d',e' and f', respectively). Titles include satellite and parameter names, along with the first-order sensitivity index S associated to each parameter.